Sustainable Energy & Fuels

ROYAL SOCIETY OF CHEMISTRY

PAPER

View Article Online
View Journal | View Issue

Cite this: *Sustainable Energy Fuels*, 2025, **9**, 5028

Wider manifestation of low-cost syringe-based printer for realizing printed organic electronic devices and supercapacitors†

Donjo George, [a] Aman Khatkar,‡[a] Vamsi Krishna G,‡[a] Lubna Khanam, [a] Yogesh Yadav, [ab] Ramesh Gupta Burela [ac] and Samarendra Pratap Singh *[a]

Additive manufacturing has emerged as an inexorable aspect in the advancement of organic electronics and energy storage technologies, especially considering the advantages of printing techniques and functional materials. Printing technology offers benefits like minimal material wastage due to its capability of pattern printing and a smooth transition from laboratory to mass production. In this context, an in-house developed, custom-built, cost-effective syringe-based printer is introduced. By controlling the extrusion amount and feed rate, thin films are optimized to achieve the desired thickness and morphology, which are crucial for high-performance, low-voltage operating Organic Field-Effect Transistors (OFETs) and Organic Solar Cells (OSCs). The printed OSC, with a device architecture of ITO/ZnO/PTB7-Th:$PC_{71}BM$/MoO_x/Ag, has achieved a Power Conversion Efficiency (PCE) of up to 6.65%, comparable to spin-coated devices of the same architecture. Additionally, the OFETs produced using this method have shown comparable charge carrier mobility of approximately 7.83×10^{-2} cm^2 V^{-1} s^{-1} and consistently higher I_{ON}/I_{OFF} ratios than the spin coated devices. Printed devices consume less material for their fabrication than spin coated devices due to selective pattern printing, and the printer can handle film thicknesses ranging from a few nanometers to micrometers. To further demonstrate the micron-level capability of the printer, a fully printed, eco-friendly, solid-state flexible supercapacitor was successfully fabricated. The supercapacitor exhibited impressive electrochemical performance, achieving a specific capacitance of 58 mF cm^{-2} at a current density of 3.00 mA cm^{-2} and an energy density of 8.00 μWh cm^{-2}. These results indicate that the low-cost syringe-based printer is a viable and superior technological alternative in the realm of flexible and printed electronics.

Received 31st May 2025
Accepted 24th July 2025

DOI: 10.1039/d5se00768b

rsc.li/sustainable-energy

1. Introduction

Organic electronics over the past few decades have experienced significant advancements, driven by the increasing demand for electronic devices that are flexible, lightweight, and cost-effective. Printed electronics is one of the promising and effective methods for sustainability, as pattern printing significantly reduces the wastage of functional materials.[1] Additionally, it minimizes the complexity of device fabrication, including frequent etching and other incumbent masking procedures, as in the case of photolithography. This approach can possibly bridge the gap between lab-scale fabrication and mass production, as manufacturing protocols, such as designing and prototyping, remain consistent across different scales.[2,3] While organic semiconductors, being solution-processable, offer unique advantages like low-temperature processing, mechanical flexibility, and tunable electronic properties,[4,5] the ink formulation for electrode materials and solution-processable biopolymers like gelatin, chitosan (serves as both gate dielectrics for OFETs, and effective separators and as polymer matrices for electrolytes), *etc.*, is potentially easier in the case of supercapacitors, and OFETs.[6–8] These characteristics make OFETs, OSCs, and supercapacitors excellent candidates for printed electronics, particularly in flexible and wearable electronics and renewable energy solutions.[9] Recent advancements in printing technologies have helped researchers to produce high-performance OFETs, OSCs, and supercapacitors, by making use of various printing techniques like inkjet printing,[10] screen printing,[11] gravure printing,[12] slot-die coating,[13] blade coating,[14] and flexographic printing.[15,16]

X. Chen *et al.* reported a record efficiency of 13.09% for PBDB-T-2F:BTP-BO-4Cl based OSCs using layer-by-layer inkjet

[a]*Department of Physics, Shiv Nadar Institution of Eminence, Gautam Buddha Nagar, Uttar Pradesh 201314, India. E-mail: samarendra.singh@snu.edu.in*

[b]*Department of Materials Science and Engineering, Technion – Israel Institute of Technology, Haifa 32000, Israel*

[c]*Department of Civil Engineering, NITTTR-Bhopal, Bhopal, Madhya Pradesh 462002, India*

† Electronic supplementary information (ESI) available. See DOI: https://doi.org/10.1039/d5se00768b

‡ These authors contributed equally.

printing.[17] Y. Liu *et al.* also reported a study based on C_6-DPA:PMMA blend-based OFETs with a charge carrier mobility of 2.01 $cm^2\ V^{-1}\ s^{-1}$.[18] Considering blade coating, L. Zhan *et al.* reported a PCE of 17.45% for a 10 mm^2 PM6:T8 based solar cell[19] while F. Wu *et al.* achieved a hole mobility of 0.54 $cm^2\ V^{-1}\ s^{-1}$ for PTTE-TVT based OFETs.[20] H Zhao *et al.* reported an efficiency of 15.6% for PM6:Y6 based OSCs[21] and Chae *et al.* demonstrated an all-3D-printed solid-state micro-supercapacitor with an energy density of 25.40 μWh cm^{-2} and a power density of 6.40 mW cm^{-2} by slot-die coating.[22] In addition to these advancements, researchers are extensively exploring the field of printed electronics.[23–27] Despite significant progress, there remains a need for a versatile system to address this field's diverse printing requirements, considering low and high ink viscosities. Therefore, in this study, a custom-built, cost-effective syringe-based printer is introduced, designed to meet these varied needs.[28] The printer employs meniscus-guided line-by-line coating (the syringe nozzle acts as the guide), like the slot-die coating process (where the die head is the guide), unlike droplet-based methods such as inkjet printing. Given the high cost of inkjet printers and other commercial alternatives, this printer offers a low-cost option with added benefits like printing a wide range of organic, inorganic, and polymer inks with varying viscosities. Numerous studies have already demonstrated that meniscus-guided printing can enhance the morphology of printed thin films.[14] When the ink forms a meniscus with the substrate, the fluid is dragged, and this unidirectional shear flow can improve the film's crystallinity and phase separation.[29–36] This method combines the advantages of both droplet-based printing (patterning capability) and meniscus-guided printing (enhanced crystallinity). Also, the ink formulation for this printer is much easier, considering the flexibility provided by varying tip sizes used for the printing process.

Herein, the capability of an in-house developed low-cost syringe-based printer is demonstrated by printing different layers of semiconducting devices like OFETs and OSCs, as well as energy storage devices like supercapacitors. The printed OSCs achieved performance comparable to spin coated ones, with a PCE of up to 6.65% for PTB7-Th:$PC_{71}BM$ based devices. Also, a similar trend was observed in the case of printed OFETs, which exhibited performance comparable to spin coated ones, with charge carrier mobilities of about $7.83 \times 10^{-2}\ cm^2\ V^{-1}\ s^{-1}$. The printed OFETs consistently showed a better ON–OFF ratio for all the devices in all cases. Furthermore, a fully printed OFET is demonstrated utilizing a gelatin biopolymer as the gate dielectric, and a fully printed supercapacitor employing a gelatin-based ionogel as the gel polymer electrolyte.

2. Syringe-based customized 3D printers

A Creality Ender Wol3D printer was procured for customization, and using its bare chassis, it was transformed into a syringe-based printer. The current modified setup replaces the conventional header of the 3D printer with a syringe mount, as shown in Fig. 1(a). All the components are labeled and shown in Fig. 1(c). The syringe with metal blunt needles and conical tips of varying gauge sizes used for printing is shown in Fig. 1(d). It is placed on the back support over the *X*-axis profile with a stepper motor that forces the piston to extrude the ink through the syringe onto the substrate placed on the print bed. A schematic showing how the syringe-based printer extrudes the ink, along with the infill pattern is shown in Fig. 1(b). Rectilinear infill patterns were employed during printing, wherein inks were deposited in parallel lines without alternating direction. This ensured uniform coverage and consistent film thickness across the printed area. Considering full coverage for thin films, the infill density is maintained at nearly 100 percent, and the build orientation is horizontal, as the printing process is planar for the discussed 2D electronic devices. The G-codes used here are those of conventional 3D printers, and a sample G-code used for printing one of the inks is given in Section S4 of the ESI.† They are modified based on the required printing pattern, extrusion, and feed rate so that the printer can control the extrusion of the inks for printing desired patterns. The printing velocity and the corresponding extruded volume are crucial to maintain the printability of the ink on the printer bed, and they are controlled using the written G-codes. For multilayer printing, a different code can be written based on the parameters needed for the subsequent film and can be loaded into the printer.

A detailed description of all the components of the syringe-based printer is given in Section S1.† Also, the rheological properties of the inks used, covering viscosity *versus* shear rate plots, storage and loss modulus *versus* shear stress, and yield stress points, are discussed in detail in Section S3.† The analysis confirms that the inks exhibit non-Newtonian shear-thinning behavior, favoring extrusion-based printing. The printing parameters for syringe-based extrusion printing include the feed rate, extrusion amount, gap height, and step size. The feed rate is the speed at which the syringe moves between the starting and ending points and is expressed in millimeters per minute (mm min^{-1}). The extrusion amount indicates the quantity of material extruded from the syringe during its motion and is expressed in mm. The relation between extrusion and the flow rate in the context of this printer is discussed in detail in Section S2.† The gap height, measured in micrometers (μm), is the constant distance between the syringe tip and the substrate throughout the printing process. Lastly, the step size, which is also expressed in mm, is the distance the syringe moves in the *x*-direction to draw two parallel lines. This step size depends on the needle gauge size and the type of ink being printed.

3. Results & discussion

3.1 Organic solar cells

To showcase the capability of the syringe-based printer, PTB7-Th:$PC_{71}BM$ active layer based OSCs are fabricated and characterized in an inverted architecture, considering their excellent stability under ambient conditions.[37–39] The energy level diagram and the corresponding device architecture of the

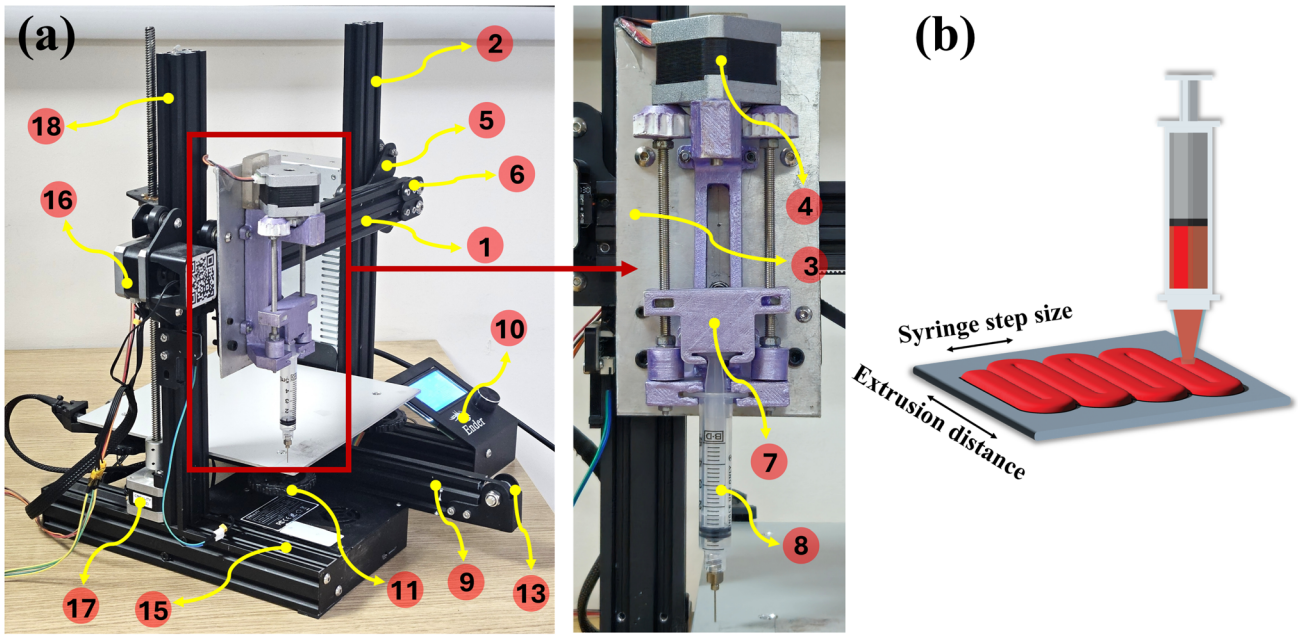

(c)

Components			
1.	X-axis profile	10.	Controller
2.	Z-axis profile (right)	11.	Hand twist level nut
3.	Support plate	12.	Print platform
4.	Stepper motor for piston	13.	Y-axis belt tensioner
5.	Z-axis passive block	14.	Power supply
6.	X-axis belt tensioner	15.	Machine base
7.	Load for piston	16.	X-axis stepper motor
8.	Syringe	17.	Z-axis stepper motor
9.	Y-axis profile	18.	Z-axis profile (left)

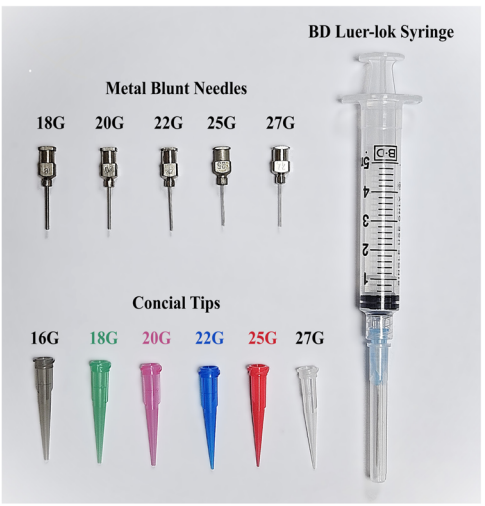

Fig. 1 Customized setup of the printer. (a) and (c) Image of the syringe-based printer labeled with its components, (b) schematic of the printing process, and (d) tips of varying sizes and the BD Luer-lok syringe used for printing.

fabricated OSC, ITO/ZnO/PTB7-Th:$PC_{71}BM$/MoO_x/Ag, are shown in Fig. 2(a and e), respectively. The donor–acceptor blend solutions in both spin coated and printed cases are made using *o*-dichlorobenzene (ODCB) as the solvent. Different syringe tips of sizes varying from 20 G to 27 G are used for initial optimization. Among these, the devices printed using a 25 G tip showed better and more consistent performance. So, in this work, 25 G is used as the standard tip size for printing both the electron transporting layer (ETL) and the active layer of the OSCs. The rheological properties of the PTB7-Th:$PC_{71}BM$ ink and ZnO inks are discussed in Section S3,† and both possess good printability as the applied stress from the syringe exceeds their yield stress. By keeping all processing conditions, like ink concentration, *etc.*, identical for both spin coating & printing, only small patches of thin films are printed, drastically reducing the amount of ink required by 1/5th compared to spin coating, on a substrate of the same area. All devices, including spin coated and printed, are fabricated and characterized under ambient conditions.

The current–voltage (*J*–*V*) curves measured for the printed and spin coated OSCs under AM 1.5 G solar irradiation are shown in Fig. 2(b) and (c). The PCE is calculated using eqn (1) as follows:

$$\mathrm{PCE}(\%) = \frac{\mathrm{FF} \times J_{sc} \times V_{oc}}{P_{in}} \times 100\% \quad (1)$$

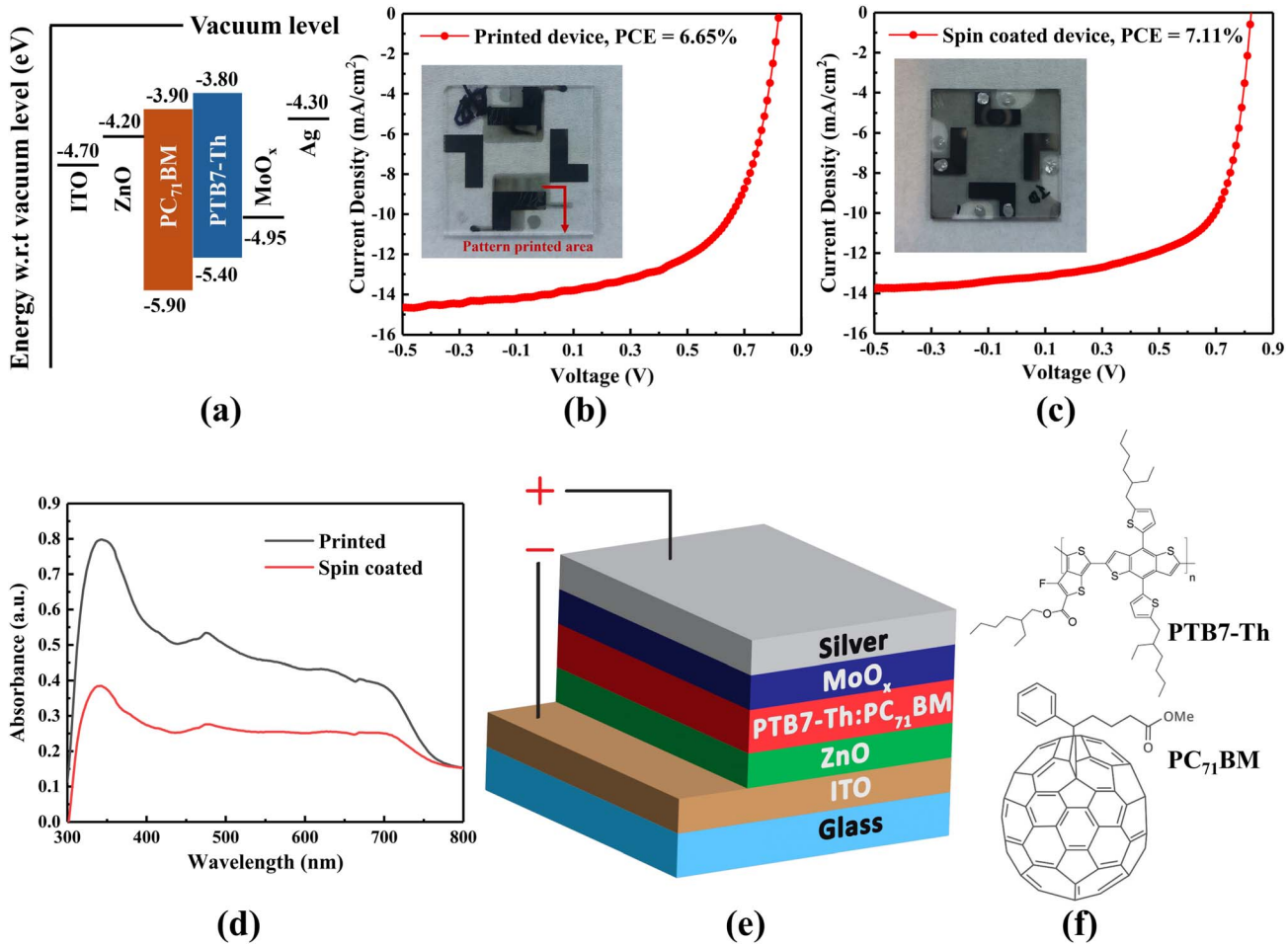

Fig. 2 Device performance and architecture of the fabricated OSCs. (a) Energy level diagram of the OSC with the architecture of ITO/ZnO/PTB7-Th:$PC_{71}BM$/MoO_x/Ag, (b) and (c) *J*–*V* curves of printed and spin coated OSCs respectively under AM1.5 G, (d) UV-vis absorption spectra of printed and spin coated OSCs, (e) device configuration used in this work, and (f) chemical structures of PTB7-Th and $PC_{71}BM$. Insets in b and c show the images of a printed and spin coated device, respectively.

where J_{sc} is the short circuit current density, V_{oc} is the open circuit voltage, P_{in} is the input solar power, and FF is the fill factor given by eqn 2

$$FF = \frac{J_{max}\ V_{max}}{J_{sc}\ V_{oc}} \quad (2)$$

where J_{max} & V_{max} are the maximum current density and voltage from *J*–*V* characteristics, respectively.[40] The AFM micrographs of ZnO and the active layer, both printed and spin coated, are shown in Fig. 3(a–d). Printed films showed more distinct grains, which could indicate better crystallinity. In contrast, spin coated films showed a finer and more uniform grain structure, suggesting a smoother surface, which was also evident from the surface roughness. The snapshot of a printed PTB7-Th:$PC_{71}BM$ thin film is also shown in Fig. 3(i). The electrical performances of printed OSCs are compared to those of spin coated OSCs and are tabulated in Table 1. The highest PCE of printed devices is 6.65%, with a short circuit current density (J_{sc}) of 13.99 mA cm^{-2}, an open circuit voltage (V_{oc}) of 0.83 V, and a fill factor (FF) value of 57.67%. The highest-performing device fabricated using spin coating showed a PCE of 7.11%, a J_{sc} of 13.30 mA cm^{-2}, a V_{oc} of 0.83 V, and an FF value of 64.82%. It is evident that the lower efficiency of the printed devices is due to their lower FF, although those devices have higher J_{sc}. The higher J_{sc} of printed devices can be attributed to the absorption spectra shown in Fig. 2(d). The thick active layer and ETL films in the printed devices result in higher absorption. While thick films contribute to higher J_{sc}, the FF might be reduced by the same thick films due to the space charge limit effect.[41,42]

3.2 Organic field-effect transistors

To further test the capability of the in-house developed syringe-based printer, OFETs based on two types of dielectrics – silicon dioxide (SiO_2) and gelatin – were fabricated and characterized, where SiO_2 was pre-integrated with the silicon (Si) substrates, and gelatin was printed.[43,44] Considering its air stability, PBTTT-C14 was selected as the active semiconducting layer. All OFET devices were fabricated in a bottom gate top contact configuration. Using the syringe-based printer, PBTTT-C14 based OFETs were fabricated and characterized by three methods: (1) OFETs having a printed active layer and thermally evaporated

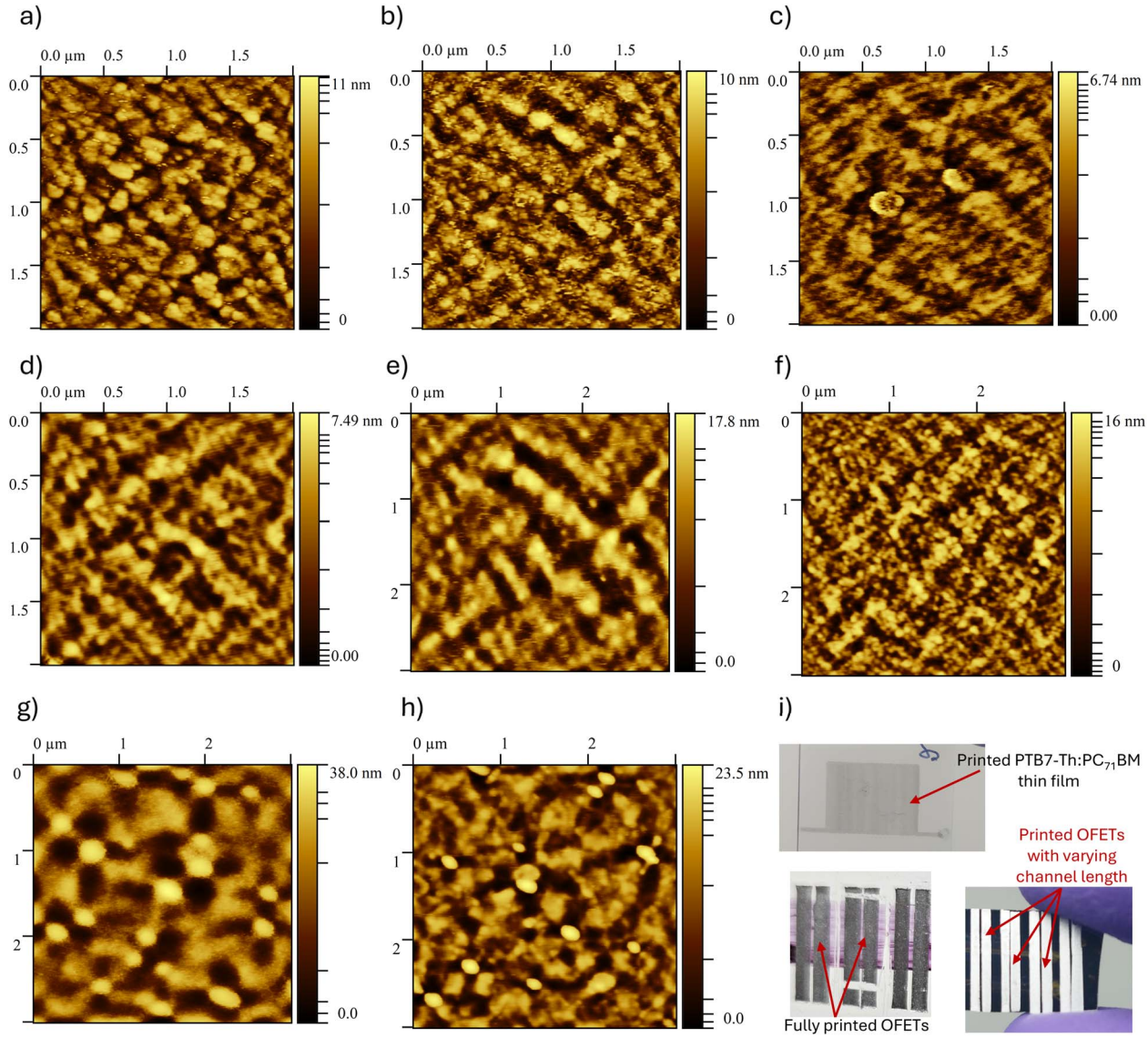

Fig. 3 AFM topographic images (2 μm × 2 μm) – (a) and (b) ZnO printed, and spin-coated respectively, and (c) and (d) PTB7-Th:$PC_{71}BM$ blend printed, and spin coated, respectively; (3 μm × 3 μm) – (e) and (f) PBTTT-C14 on gelatin/ITO printed and spin coated, respectively; (g) and (h) PBTTT-C14 on OTS-treated Si/SiO_2 printed and spin coated, respectively and (i) snapshots (top–bottom clockwise) of printed PTB7-Th:$PC_{71}BM$ thin films on a glass substrate, OFETs with printed PBTTT-C14 and top S-D electrodes using Ag ink with OTS-treated SiO_2 as the gate dielectric, and OFETs with all the layers printed, including gelatin gate dielectric, PBTTT-C14 active layer, and top S-D Ag electrodes.

gold (Au) top source-drain (S-D) electrodes with trichloro(octadecyl)silane (ODTS) treated SiO_2 as the gate dielectric, (2) OFETs having a printed active layer and printed top S-D electrodes using silver (Ag) ink with trichloro(octyl)silane (OTS) treated SiO_2 as the gate dielectric and (3) fully printed OFETs with the same active layer, gelatin as the gate dielectric and printed top S-D electrodes using Ag ink.

Table 1 Photovoltaic parameters of PTB7-Th:$PC_{71}BM$-based OSCs under AM 1.5 G illumination, 100 mW cm^{-2}

Thin film technique	V_{oc} (V)	J_{sc} (mA cm^{-2})	P_{max} (mW cm^{-2})	FF (%)	PCE[a] (%)	R_s (ohms)	R_{sh} (ohms)	Thickness (nm)
Printed	0.83	−13.99	−6.65	57.67	6.65 (6.16 ± 0.4)	86	5272	102
Spin coated	0.83	−13.30	−7.11	64.82	7.11 (6.69 ± 0.33)	63	3027	93

[a] The average PCE values and standard deviations were obtained for 5 different devices.

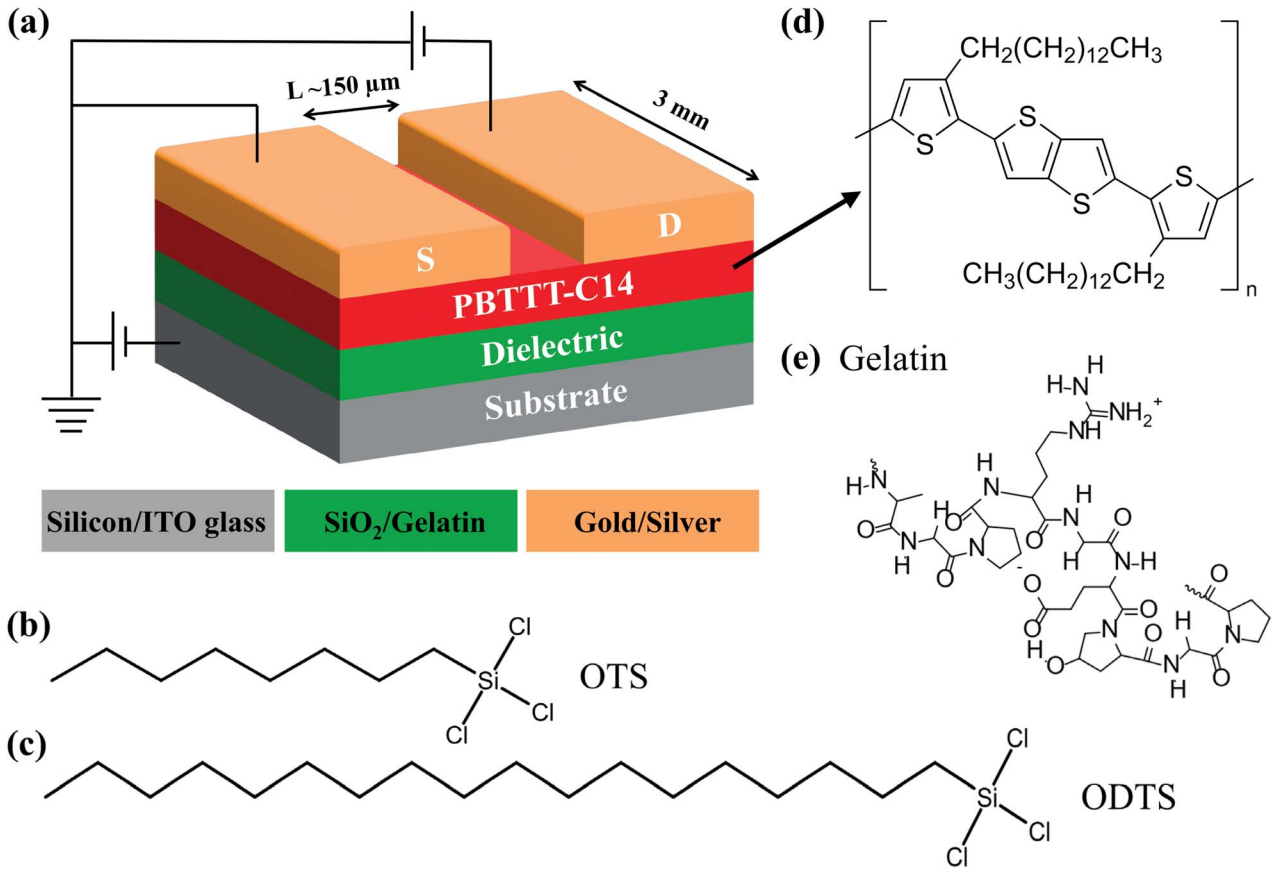

Fig. 4 (a) General schematic of the OFETs used in this work, (b) chemical structure of OTS, (c) ODTS, (d) PBTTT-C14, and (e) gelatin.

All the printed devices were pattern printed, reducing the material usage by 1/5th of that required to fabricate a spin coated OFET. Indium Tin Oxide (ITO) coated substrates are used for fully printed OFET devices. The OFET architecture and the chemical structures of all materials used in this work are shown in Fig. 4(a–e). The rheological properties of the Ag ink are discussed in Section S3,† and they exhibit non-Newtonian shear-thinning, favoring smooth extrusion. The snapshots of OFETs with a printed active layer, printed top electrodes, and a fully printed OFET are shown in Fig. 3(i). The performance of all printed devices is compared to that of conventionally fabricated devices, where spin coating is used for the semiconductor layer and thermal deposition is used for the source and drain electrodes.

3.2.1 Figure of merit of the OFETs. The printed OFETs were characterized, and their transfer (I_{ds}–V_{gs}) and output characteristics (I_{ds}–V_{ds}) were plotted for all OFET devices, as shown in Fig. 5–7(a–d). The following electrical figures of merit are also extracted from the current–voltage characteristics. The charge carrier mobility can be determined from the saturation regime

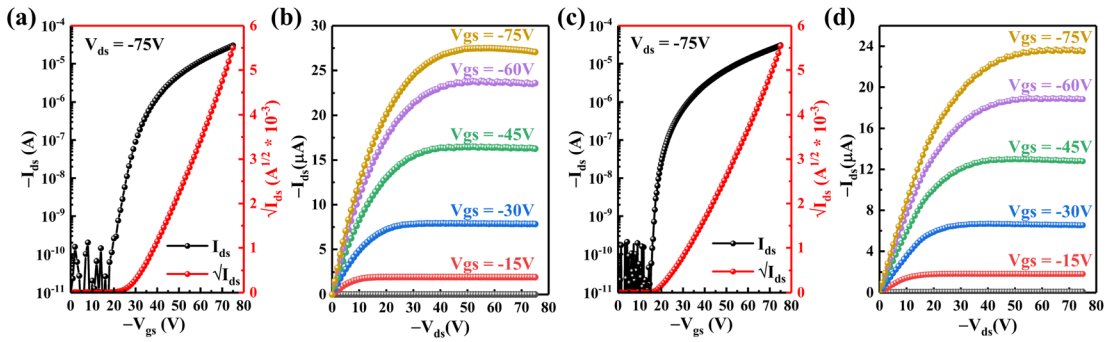

Fig. 5 (a) and (c) The transfer characteristics of spin coated and printed OFETs, respectively, where only the processing of the active layer is considered for comparison, and (b) and (d) the output characteristics of the same devices.

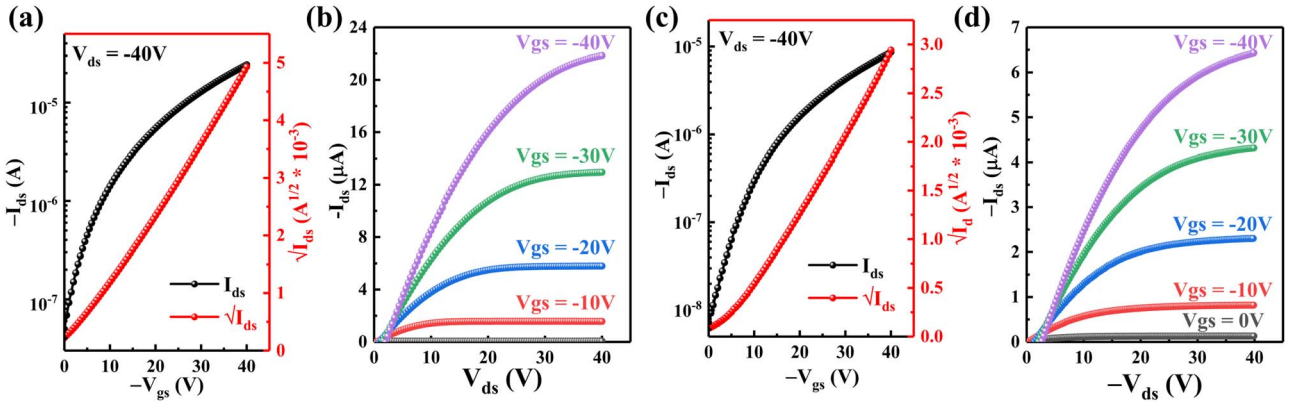

Fig. 6 (a) and (c) The transfer characteristics of spin coated and printed OFETs, respectively, where the processing of the active layer & top S–D electrodes is considered for comparison, and (b) and (d) the output characteristics of the same devices.

($V_{ds} \geq V_{gs}$).[45,46] It was directly extracted by finding the slope of the linear fit of the $\sqrt{I_{ds}}$ vs V_{gs} curve by using eqn (3):[47]

$$I_{ds} = \frac{W}{2L}\mu_{sat} C_{sp}\left(V_{gs} - V_{th}\right)^2 \quad (3)$$

where I_{ds} is the current across the source and drain electrodes, V_{gs} is the gate voltage across the gate and source electrodes, V_{th} is the threshold voltage, indicating the minimum gate voltage required to make the charge carriers in the channel mobile, C_{sp} is the specific capacitance of the gate dielectric used, W is the channel width, L is the channel length and μ_{sat} is the charge carrier mobility in the saturation regime. The threshold voltage (V_{th}) can also be found using the exact linear fit of the $\sqrt{I_{ds}}$ vs V_{gs} curve, where its intercept with the x-axis gives the V_{th} of the transistor. The on–off ratio (I_{ON}/I_{OFF}) is the ratio of drain current I_{ds} at a certain V_{gs} applied and I_{ds} typically at $V_{gs} = 0$. The sub-threshold swing (SS) is estimated using eqn (4) as follows:[48]

$$SS = \left.\frac{\partial V_{gs}}{\partial(\log_{10} I_{ds})}\right|_{V_{gs}} \quad (4)$$

Using the sub-threshold slope, the interfacial trap density between the semiconducting & dielectric layer can be theoretically determined by using eqn (5). The upper limit to interfacial trap density is given by

$$N_{it}^{max} \approx \left[\frac{q\ SS \log(e)}{k_B\ T} - 1\right]\frac{C_{sp}}{q} \quad (5)$$

where q is the electronic charge.[49] Also, transconductance and contact resistance are two other essential parameters for evaluating OFET performance, especially considering this work compared to different thin film fabrication techniques.[45] The transconductance shows how output current varies in response to the input voltage and is estimated using eqn (6) as follows:[50]

$$g_m = \left(\frac{\partial I_{ds}}{\partial V_{gs}}\right)_{V_{ds}} \quad (6)$$

The contact resistance (R_C) can be extracted from the output characteristics of the OFET using the transition voltage method (TVM)[51] and is given by eqn (7) as follows

$$R_C = \frac{2\sqrt{\left(V_{gs} - V_{th}\right)}\left(\sqrt{2V_{tr}} - \sqrt{\left(V_{gs} - V_{th}\right)}\right)}{I_{ds,sat}} \quad (7)$$

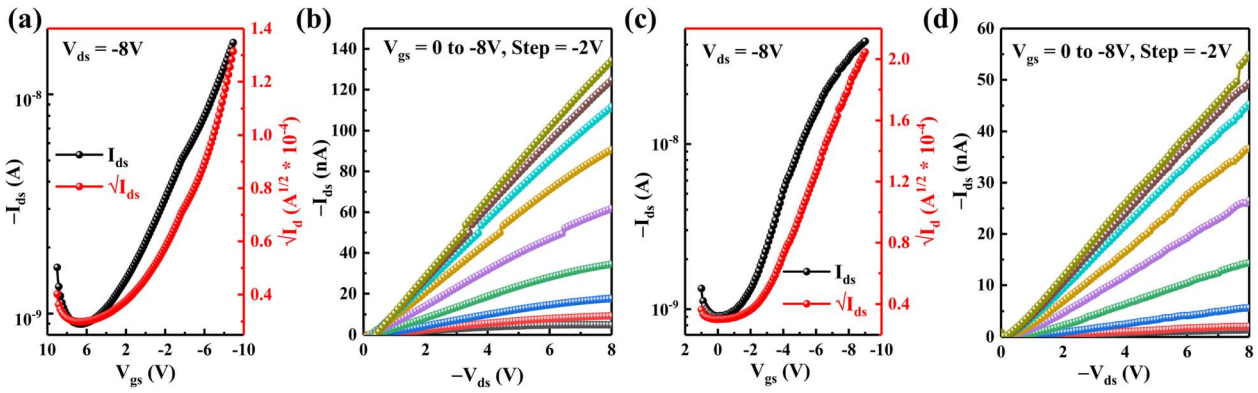

Fig. 7 (a) and (c) The transfer characteristics of spin coated and fully printed OFETs, respectively, where the processing of the dielectric layer, active layer & top S–D electrodes is considered for comparison, and (b) and (d) the output characteristics of the same devices.

Table 2 Figure of merit of spin coated and printed OFETs, where the processing of the active layer is only considered for comparison

Device configuration	Substrate	Mobility ($cm^2 V^{-1} s^{-1}$) ($\times 10^{-2}$)	Threshold voltage (V)	ON–OFF ratio	Sub-threshold swing (V per decade)
PBTTT-C14 – spin coated, Au – thermally deposited	ODTS treated n^{++} Si/SiO_2	9.10	−26.34	2.51×10^5	2.75
PBTTT-C14 – printed, Au – thermally deposited	ODTS treated n^{++} Si/SiO_2	7.83	−20.32	3.75×10^5	1.18

Table 3 Figures of merit of spin coated and printed OFETs, respectively, where the processing of the active layer & top S–D electrodes is considered for comparison

Device configuration	Substrate	Mobility ($cm^2 V^{-1} s^{-1}$)	Threshold voltage (V)	ON–OFF ratio	Sub-threshold swing (V per decade)
PBTTT-C14 – spin coated, Ag – thermally deposited	OTS treated n^{++} Si/SiO_2	1.33×10^{-1}	−1.14	4.87×10^2	3.78
PBTTT-C14 – printed, Ag – printed	OTS treated n^{++} Si/SiO_2	6.61×10^{-2}	−6.43	1.20×10^3	5.20

where V_{tr} is the transition voltage, and $I_{ds,sat}$ is the current at that voltage. V_{tr} gives an idea about the point at which the output characteristics transition from the linear to the saturation regime. The subsequent sections will discuss all the parameters mentioned above for the devices fabricated.

3.2.2 Printed PBTTT-C14 and thermally deposited S–D electrodes. In this section, the performances of OFET devices with an active layer printed with spin coated devices are compared. The transfer and output characteristics of the printed and spin coated OFETs are shown in Fig. 5(a–d). All the electrical figures of merit are summarized in Table 2. It is observed that both devices exhibit comparable charge carrier mobilities on the order of $\sim 10^{-2}$, although spin coated devices have slightly higher mobility in magnitude. This can be attributed to the lower transconductance values of ~1.02 μS and higher contact resistance values of ~0.44 MΩ of the printed OFETs. The devices with spin coated PBTTT-C14 exhibited a higher transconductance value of ~1.65 μS and a lower contact resistance of ~0.22 MΩ. Contact resistance acts as a bottleneck for charge injection from the contacts into the semiconductor.[52,53] Higher transconductance indicates that a slight change in gate voltage results in a significant change in drain current, which implies that the charge carriers move more efficiently through the channel, which is a direct indicator of higher mobility.[54] The printed device has an excellent sub-threshold slope at lower values of ~1.18 V per decade, which can lower the threshold voltage as the transistor reaches the conduction threshold more quickly as the gate voltage increases. The lower sub-threshold swing observed in the printed devices can be attributed to their lower interfacial trap density of around $\sim 1.37 \times 10^{12}$ cm^{-2}, compared to spin coated devices ($\sim 3.28 \times 10^{12}$ cm^{-2}). Printing might have resulted in a smoother and cleaner interface, which is the reason for reduced trap states, directly contributing to the lower sub-threshold swing.

3.2.3 Printed PBTTT-C14 and top S–D electrodes. In this section, the electrical performance is discussed for OFET devices with a printed active layer and printed top S–D electrodes compared to OFET devices with a spin coated active layer and thermally deposited S–D electrodes, summarized in Table 3. The transfer and output characteristics of the printed and spin coated OFETs are shown in Fig. 6(a–d). The printed devices performed similarly to the conventionally spin coated devices. The lower mobility can be attributed to its lower transconductance values of ~0.54 μS and a higher contact resistance of ~2.56 MΩ. The spin coated devices showed a transconductance of ~1.3 μS and a lower contact resistance of ~0.37 MΩ. The printed devices showed an excellent on-off ratio on the

Table 4 Figures of merit of spin coated and printed OFETs, respectively, where the processing of the active layer, dielectric layer & top S–D electrodes is considered for comparison

Device configuration	Substrate	Mobility ($cm^2 V^{-1} s^{-1}$) ($\times 10^{-2}$)	Threshold voltage (V)	ON–OFF ratio	Sub-threshold swing (V per decade)
Gelatin – spin coated, PBTTT-C14 – spin coated, and Ag – thermally deposited	ITO coated glass	1.39	−1.26	8.38	10.20
Gelatin – printed (12 layers), PBTTT-C14 – printed, and Ag – printed	ITO coated glass	4.94	−1.56	45.98	9.30

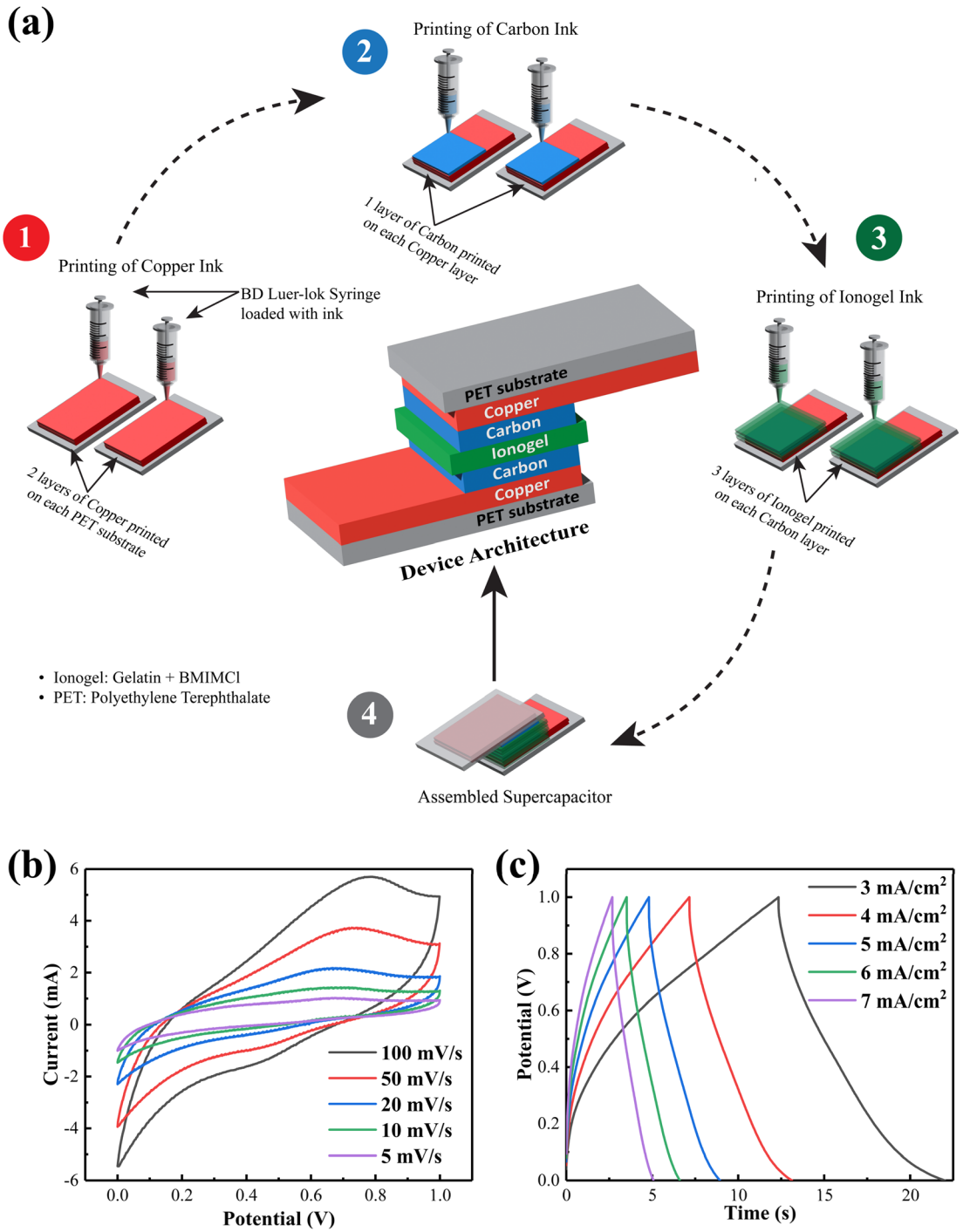

Fig. 8 (a) Detailed schematic showing all the processes involved in supercapacitor fabrication, (b) cyclic voltammogram and (c) galvanostatic charge–discharge curves of the fabricated supercapacitor.

order of ~10^3. However, the interfacial trap density was around ~6.27×10^{12}, which is slightly higher compared to the spin coated devices' trap density, around ~4.54×10^{12}. The AFM micrographs of PBTTT-C14 films on the OTS-treated Si/SiO_2 substrate, both printed and spin coated, are shown in Fig. 3(g and h), and a snapshot of the fabricated OFET is shown in Fig. 3(i). Applying bed temperature while printing PBTTT-C14 made the films rougher, which is evident from the AFM micrographs, and it is further reflected in increased trap density.

3.2.4 Fully printed OFETs with a biopolymer gate dielectric. This section compares the electrical performances of fully printed OFETs to those of devices with a spin-coated active layer and thermally deposited S–D electrodes, which are tabulated in Table 4. The transfer and output characteristics of the printed and spin coated OFETs are shown in Fig. 7(a–d). The printed

devices showed higher charge carrier mobility and a higher on–off ratio, which can be ascribed to higher transconductance values of ~8.98 nS. In comparison, spin coated devices have a lower transconductance value of ~4.77 nS. The TVM method for finding contact resistance becomes ineffective in the case of these devices, as the output characteristics don't show a prominent transition from the linear to the saturation regime. The fully printed devices exhibited trap densities of $\sim 1.13 \times 10^{13}$ cm^{-2}, whereas the conventional spin coated devices showed values of $\sim 1.24 \times 10^{13}$ cm^{-2}. The AFM micrographs of PBTTT-C14 films on the gelatin/ITO glass substrate, both printed and spin coated, are shown in Fig. 3(e and f), along with a snapshot of the fabricated OFETs in Fig. 3(i). Here, the printed films showed distinct grains while spin coated devices showed finer and smoother films. Also, the development of water-soluble biopolymers as gate dielectrics for low voltage operating OFETs has the potential to offer low power requirements for electronic functions. Such prospects align with Sustainable Development Goal 7, which is about universal access to affordable, reliable, and sustainable energy.

3.3 Supercapacitors

Considering the applicability of the printer is crucial in a wide window of flexible and printed electronics, and to substantiate this, a fully printed supercapacitor is fabricated and characterized in which all the layers, from metal contacts to gel polymer electrolytes, are printed. A detailed schematic showing the device architecture and all the processes involved in the fabrication process is shown in Fig. 8(a). Micron-level film thickness can be easily achieved through multilayer printing and by controlling the printing parameters. The electrode material used here is carbon ink, and copper ink is used for the metal contacts. The electrolyte used is gelatin-ionic liquid based ionogel, which has been used as a gel polymer electrolyte. The ionic liquid used here is 1-butyl-3-methylimidazolium chloride

Table 5 Comparison of reported studies based on syringe-based printing

Printer setup	Applications	Printed films (thickness)		Performance	Limitations	Ref.
Syringe-based extrusion using a Creality Ender 3 Pro printer	Solar cells	PEDOT:PSS (142 nm) and $MAPbI_{3-x}Cl_x$ perovskite (NA)		NA	High-viscosity inks are not covered	26
Pneumatic nozzle-based setup interfaced with Nordson EFD pressure controller	OFETs	TIPS-pentacene (NA) and Ag (NA)		Mobility: 8×10^{-1} cm^2 V^{-1} s^{-1}	Application over a limited range of film thicknesses demonstrated	55
Syringe-based extrusion using a Hyrel3D 30M printer	Supercapacitors	Activated carbon (500 μm) and PVA/H_3PO_4 (~100 μm)		329 mF cm^{-2} at 2.5 mA cm^{-2}	Limited scope for printing low-viscous inks	27
	Composite materials for 3D printing	PDMS composite (50 μm), HDPE filament composites (NA), *etc.*		NA		56 and[57]
Syringe-based extrusion using image master 350 PC smart 3-axis dispenser	Supercapacitors	Nickel composite current collector (30 μm), graphene composite electrode (NA), and EMIM TFSI composite electrolyte (NA)		20.4 mF cm^{-2} at 0.5 mA cm^{-2}		22
	Stretchable conductors, electrodes, *etc.*, for electronic devices	PVP-functionalized eutectic gallium indium composites (NA), Ag inks (NA), *etc.*		NA		58 and[59]
Syringe-based extrusion using a Creality Ender Wol3D Printer	OSCs, OFETs, and supercapacitors	ETL	ZnO (26 nm)	OSC PCE: 6–7%, OFET mobility: (0.14–1.33) × 10^{-1} cm^2 V^{-1} s^{-1}. Supercapacitor capacitance: 58 mF cm^{-2}	High precision printing of resolutions less than 50 μm is to be improved	This work
		Device active layers	PTB7-Th:$PC_{71}BM$ (76 nm) & PBTTT-C14 (40 nm)			
		Metal contacts	Ag (30 μm) & copper[a] (150 μm)			
		Gate dielectric	Gelatin (20 mg mL^{-1})[a] (200 nm)			
		Electrode	Carbon (35 μm)			
		Gel–polymer electrolyte	Gelatin ionogel (50 mg mL^{-1})[a] (80 μm)			

[a] indicates the thickness for 1 layer; NA indicates not available.

(BMIMCl). The rheological properties of carbon ink and ionogel are discussed in Section S3†, and they were found to exhibit favorable shear-thinning properties. All the layers were printed on a flexible PET substrate sequentially.

Cyclic voltammetry and galvanostatic charge–discharge studies were performed on the fully printed supercapacitors, as shown in Fig. 8(b and c). The fabricated devices showed pseudocapacitive behavior, as evident from the redox peaks in the CV curves at different scan rates. Device figures of merit were calculated using both CV and GCD techniques.

Using CV,

$$C_s = \frac{2\int I\,dV}{m\nu\Delta V} \quad (8)$$

Using GCD,

$$C_s = \frac{2\int I\,dt}{A\Delta V} \quad (9)$$

where $\int I\,dV$ is the area enclosed by the CV curve, m (g) is the total mass of the electrode loaded, ν (V s^{-1}) is the scan rate, A (cm^2) is the area of the electrode, ΔV is the range of potential, I (A) is the discharge current and dt (s) is the discharge time.

The device exhibited areal capacitance values of 58, 47, 41, 37, and 33 mF cm^{-2} at current densities of 3, 4, 5, 6, and 7 mA cm^{-2}, respectively. Gravimetric capacitance values, derived from CV curves at scan rates of 100, 50, 20, 10, and 5 mV s^{-1}, were calculated to be 32, 44, 63, 81, and 108 F g^{-1}, respectively. The equivalent series resistance (ESR) was measured at 13 Ω, with an iR drop of 0.04 V. The lower ESR highlights the potential of the developed ionogel and its excellent contact with the electrodes, demonstrating the printer's capability to produce high-quality, micron-level, multi-layer gel polymer electrolytes. The energy density of the supercapacitor was determined to be 8 μWh cm^{-2} using the formula $E = \frac{CV^2}{2 \times 3600}$, and the power density was calculated to be 3 mW cm^{-2} using $P = \frac{3600 \times E}{dt}$.

To better understand the scope of this work, the application of syringe-based extrusion printing across various electronic devices is reviewed. Table 5 compares film thickness achieved by different printer setups from previous studies. While most of these studies have produced only a few micron-thick films, thin films in the nanometer range are crucial for printed electronics. The syringe-based printer discussed in this work can handle film thicknesses ranging from a few nanometers all the way up to hundreds of micrometers, as demonstrated by the successful printing of good-quality electronic thin films. Achieving a wide range of film thicknesses with a single printer setup demonstrates significant versatility and adaptability, as the metal electrode and biopolymer printing are optimized. This capability is particularly valuable for tailoring electronic properties to specific applications like those discussed, thereby enhancing the performance and functionality of printed electronic devices. Moreover, the cost of procuring such a printer is much less than that of expensive alternatives that are currently available on the market. However, certain limitations remain. The printer's spatial resolution, less than 50 μm for high-precision microelectronics, must be improved. Low-viscosity inks may require additional optimization to prevent spreading, while inks formulated with highly volatile solvents might face challenges like clogging, inconsistent extrusion, or non-uniform film formation, especially under ambient conditions during the printing process. These limitations highlight areas for future improvement while underscoring the importance of precise control over film thicknesses and the capability of the in-house developed syringe-based printer in developing printed and flexible electronics.

4. Conclusions

A low-cost syringe-based printer has been introduced, which can be an excellent substitute for expensive alternatives currently available on the market. Using the syringe-based printer, its abilities in two broad areas of semiconducting devices, including OSCs and OFETs, were showcased. By controlling the substrate temperature, feed rate, extrusion amount, and printing nozzle size, films of good electronic quality from a few nanometers to micrometers were printed for the above two cases. Using the printer, comparable performances of PTB7-Th:$PC_{71}BM$ active layer based OSCs and PBTTT-C14 based OFETs were demonstrated. The printed OSCs in which the ZnO ETL and PTB7-Th active layer were printed showed performance comparable to that of the control devices fabricated using conventional methods like spin coating and thermal deposition techniques. The printed OSCs fabricated in ambient air showed a PCE of up to 6.65%, whereas the control devices showed a PCE of up to 7.11%. To further show the printer's capability, PBTTT-C14 based low-voltage operating OFETs were fabricated and characterized in ambient air, showing a comparable electrical figure of merit to that of spin coated devices. The printed OFETs showed consistent mobility on the order of $\sim 10^{-2}$ cm^2 V^{-1} s^{-1}, whereas the conventionally fabricated OFETs using spin coating showed mobilities in the range of $\sim 10^{-2}$ – 10^{-1} cm^2 V^{-1} s^{-1}. The printed OFETs consistently showed a better ON–OFF ratio than the control devices in all cases. The fully printed OFETs utilizing a gelatin biopolymer as the gate dielectric also exhibited similar performance. Furthermore, to demonstrate the syringe-based printer's capability in producing micron-level thick films, a fully printed eco-friendly supercapacitor was fabricated using a gelatin-based ionogel as the gel polymer electrolyte. This fully printed supercapacitor achieved an impressive areal capacitance of 58 mF cm^{-2} and a gravimetric capacitance of 108 F g^{-1}. These findings underscore the potential of the in-house developed syringe-based printer in the realm of flexible and printed electronics. The printer excels in minimizing material consumption by selective pattern printing and is adept at printing a wide range of inks, from low-viscosity organic polymer-based solutions to high-viscosity inks like Ag, carbon, and biopolymers such as gelatin-based solutions.

5. Experimental details

5.1 Materials

All solvents and chemicals were used without further purification and obtained commercially. PTB7-Th (poly{4,8-bis[5-(2-ethylhexyl)thiophen-2-yl]benzo[1,2-*b*:4,5-*b*′]-dithiophene-2,6-diyl-*alt*-3-fluoro 2-[(2-ethylhexyl)carbonyl]-thieno[3,4-*b*] thiophene-4,6-diyl}), $PC_{71}BM$ ([6,6]-phenyl-C71-butyric acid methyl ester) and ITO glasses with ~15 Ω cm^{-2} sheet resistance were purchased from Lumtec (Luminescence technology corp., Taiwan). PBTTT-C14 (poly[2,5-bis(3-tetradecylthiophen-2-yl) thieno[3,2-*b*]thiophene]), ODCB, 2-methoxy ethanol, ethanolamine, zinc acetate dihydrate, OTS, ODTS, gelatin, and BMIMCl were purchased from Sigma-Aldrich Co. Ag ink was purchased from Techinstro Industries, India. Carbon and copper ink were purchased from Likhatronics, India. Molybdenum(VI) oxide (MoO_3, 99.95% sublimed powder), gold (Au, 99.995% shots), and Ag (99.99% wire) were purchased from Alfa-Aesar, USA. Heavily doped *n*++ silicon (Si) wafers with thermally grown 200 nm silicon dioxide (SiO_2) were purchased from Wafer Pro, USA.

Table 6 summarizes the printing parameters for all the inks used in this work. These were optimized by comparing the performances of different electronic devices, their consistency, and film morphologies. All the inks used in this work were loaded into a 5 mL Luer-lok syringe attached to a corresponding nozzle for printing. The rheology analysis for the inks used was carried out using a controlled-stress rheometer MCR302e from Anton Paar, Austria. All the AFM images were captured using an MFP-3D Origin AFM system from Oxford Instruments, UK. The thicknesses of various films were measured using a surface profilometer, DektakXT from Bruker, USA.

5.2 Fabrication & characterization of OSCs

The architecture of the devices was glass/ITO/ZnO/PTB7-Th:$PC_{71}BM$/MoO_x/Ag. ITO-coated glasses were cleaned sequentially in a Labolene-based detergent solution, de-ionized (DI) water, acetone, and isopropyl alcohol (IPA) by sonication, and were dried thereafter before being subjected to UV-Ozone treatment. ZnO was prepared using the sol–gel process in which 0.5 M zinc acetate dihydrate precursor and 0.5 M ethanolamine were dissolved in 2-methoxy ethanol by sonicating it for one hr. at 50 °C. The prepared ZnO solution was spin coated at 3000 rpm for 60 seconds, and the same solution was used as the ZnO ink. The ZnO thin films, both printed and spun, were annealed at 150 °C for 15 minutes. PTB7-Th and $PC_{71}BM$ were weighed correctly to maintain a total concentration of 23 mg mL^{-1} in a 1:1.5 donor–acceptor (D-A) ratio. ODCB solvents were then added separately in a 6:4 ratio for donor and acceptor solutions, respectively, and the mixtures were stirred at 90 °C, 420 rpm for 19 hours. Later, these solutions were mixed and blended by stirring for another 2 hours. 3 vol% DIO was added and stirred for 30 minutes. The prepared D–A blend solutions were spin coated on top of the ZnO thin film at 900 rpm for 90 seconds, and the same solution was used as the PTB7-Th:$PC_{71}BM$ ink. The spin coated and printed devices were dried in a nitrogen environment for 45 minutes. Later, these devices were loaded into a thermal evaporator, and MoO_3 & Ag were sequentially deposited under high vacuum (~10^{-6} mbar) using shadow masking. The active layer's thickness was around 93 nm for spin coated devices and 102 nm for printed devices. For both printed and spin coated devices, the active area of the solar cell was fixed at 9 mm^2.

The current–voltage (*I*–*V*) characterization was carried out in an ambient environment (45% RH at 25 °C) using a Keithley 2450 SMU under solar irradiance of AM 1.5 G or 100 mW cm^{-2} using a solar simulator (Model: SSS50AAA) with a Xenon-Arc lamp from Photo Emission Tech. (PET) Inc., California, calibrated using a standard NREL Si solar cell. Absorbance spectroscopy was carried out using an ultraviolet-visible–near-infrared (UV-vis-NIR) spectrophotometer from Shimadzu (SolidSpec 3700).

5.3 Fabrication & characterization of OFETs

For devices based on SiO_2 as the gate dielectric and PBTTT-C14 as the semiconducting layer, the same procedure was used as in previous studies to fabricate these devices.[43] In devices with OTS treatment, PBTTT-C14 was printed at a prolonged feed rate of 5 mm min^{-1} while heating the substrate at 60 °C. This was done to ensure proper adhesion of ink drops to the OTS-treated

Table 6 Optimized printing parameters for various inks used in this work

Material	Nozzle size	Feed rate (mm min^{-1})	Extrusion (mm)	Step size (mm)	Bed temperature (^{O}C)	Gap height (μm)
ZnO	25 G	50	0.01	0.5	—	75
PTB7-Th:$PC_{71}BM$	25 G	20	0.02	0.4	—	50
PBTTT-C14 on Si/SiO_2 substrate	25 G	20	0.01	0.4		50
PBTTT-C14 on OTS-treated Si/SiO_2 substrate	25 G	5	0.01	0.4	80	50
Ag	20 G	20	0.5	—	—	100
Gelatin (20 mg mL^{-1})	20 G[a]	50	0.5	0.8	—	75
Copper	18 G	50, 100	1,2	0.8	—	125
Carbon	18 G	50	1	0.6	—	100
Ionogel	18 G[a]	50	2	0.8	—	150

[a] Indicates that the nozzle used is a conical plastic tip, while it is a metal blunt needle in all other cases.

surface, as they are slightly phobic to ODCB-based inks. As a result, the final films were rough compared to other printed films. Here, in this case, Ag was used as the top S–D electrodes for comparison, in contrast to the previous work referred to. The thermally deposited Ag S–D electrodes using shadow masks were designed to achieve a 3 mm channel width and a 150 μm channel length for each device. In comparison, two lines of Ag ink were printed in parallel, with a length of 3 mm on top of PBTTT-C14 films, resulting in a channel width of 3 mm, and a channel length of 149 μm.

For devices with a gelatin biopolymer as the gate dielectric, the same procedure as the control devices in the previously reported work was followed.[44] A gelatin concentration of 20 mg mL^{-1} in deionized water (DI) was used for printing, and to match the dielectric thickness of spin coated devices, where the concentration was 250 mg mL^{-1}, 12 layers of gelatin were printed sequentially, one after the other, with a 5-minute drying time at 50 °C. The 20 mg mL^{-1} solution was stable for printing even longer, as it remained without solidification. The printed and spin coated gelatin films (12 layers) showed thicknesses of about 2 μm. For printing PBTTT-C14, the same criteria as before were used. Here also, Ag was used as the top S–D electrodes for comparison, in contrast to the previously referred work. The same criteria were used as before for the top electrodes in fully printed devices.

The current–voltage characterization and specific capacitance measurements were carried out as previously reported.[43] The electrical characterization was conducted using a Keithley 4200-SCS in an ambient environment (45% RH at 25 °C). The capacitance measurements were performed using an LCR Meter (Model: ZM2376) from NF Corporation, Japan.

5.4 Fabrication & characterization of supercapacitors

The fabrication process of the fully printed supercapacitor involves multiple steps. Initially, copper (Cu) ink was printed onto a polyethylene terephthalate (PET) substrate with printing area dimensions of 2 cm in length and 1 cm in width. Two layers of Cu ink were printed: the first layer was printed along the width, while the second layer was printed along the length. The printed Cu layers were then sintered at 100 °C for 2 hours. Subsequently, carbon ink was printed on top of the Cu layer over an area of 1 cm^2. This layer was sintered at 60 °C for 30 minutes.

For the ionogel layer, gelatin + BMIMCl ionogel ink was prepared by first dissolving 5 wt% BMIMCl in DI water at 60 °C for 30 minutes. Gelatin was then added to the aqueous ionic liquid (IL) solution at a concentration of 5% (w/v) and mixed for an additional hour at the same temperature. The resulting ionogel was printed over an area of 1.2 cm by 1.2 cm on top of the carbon layer. This layer was allowed to dry at room temperature for 15 minutes, followed by the printing of two additional layers using the same protocol.

Cu, carbon, and ionogel layers were printed in the sequence on another PET substrate. Both substrates were then left to dry at room temperature for 12 hours. Finally, the two substrates were sandwiched together and packed to form a fully printed supercapacitor.

The cyclic voltammetry and galvanostatic charge–discharge cycle measurements were performed on a single device by using an Electrochemical Workstation from CH Instruments (Model: CHI600F), USA, in an ambient environment (45% RH at 25 °C).

Data availability

All data supporting this study's findings are included in the article and any ESI.†

Author contributions

Donjo George: data curation; formal analysis; investigation; methodology; software; validation; visualization; writing – original draft; writing – review & editing. Aman Khatkar: data curation; investigation; methodology; software. Vamsi Krishna G: data curation; investigation; methodology; software. Lubna Khanam: formal analysis; investigation; methodology. Yogesh Yadav: formal analysis; investigation; methodology. Ramesh Gupta: conceptualization; methodology; project administration; resources; software; supervision. Samarendra Pratap Singh: conceptualization; formal analysis; funding acquisition; investigation; methodology; project administration; resources; software; supervision; validation; visualization; writing – review & editing.

Conflicts of interest

There are no conflicts to declare.

Acknowledgements

The authors thank the Shiv Nadar Institution of Eminence (SNIoE) and the Shiv Nadar Foundation for the financial support through the doctoral fellowship. D. G. thanks Ms. Ushasri Mukherjee, Ms. Feba Elsa George, and Dr Bishwajit Mandal for their help in learning instruments and characterization techniques. The authors acknowledge Dr Arpan Bhattacharyya, Dr Sajal Ghosh, Dr Rakesh Sharma, and Mr Vijay Sharma for their support during the experimental arrangements. S.P.S. acknowledges financial support from the grant DST-SERI/S-127.

References

1 P. Martins, N. Pereira, A. C. Lima, A. Garcia, C. Mendes-Filipe, R. Policia, *et al.*, Advances in Printing and Electronics: From Engagement to Commitment, *Adv. Funct. Mater.*, 2023, **33**(16), 2213744, DOI: **10.1002/adfm.202213744**.

2 J. Wiklund, A. Karakoç, T. Palko, H. Yiğitler, K. Ruttik, R. Jäntti, *et al.*, A Review on Printed Electronics: Fabrication Methods, Inks, Substrates, Applications and Environmental Impacts, *J. Manuf. Mater. Process.*, 2021, **5**(3), 89, DOI: **10.3390/jmmp5030089**.

3 D. Maddipatla, B. B. Narakathu and M. Atashbar, Recent Progress in Manufacturing Techniques of Printed and Flexible Sensors: A Review, *Biosensors*, 2020, **10**(12), 199, DOI: 10.3390/bios10120199.
4 S. Duan, B. Geng, X. Zhang, X. Ren and W. Hu, Solution-processed crystalline organic integrated circuits, *Matter*, 2021, **4**(11), 3415–3443, DOI: 10.1016/j.matt.2021.09.002.
5 L. Sun, Y. Chen, M. Sun and Y. Zheng, Organic Solar Cells: Physical Principle and Recent Advances, *Chem Asian J*, 2023, **18**(5), e202300006, DOI: 10.1002/asia.202300006.
6 S. Chaichana, P. Iamprasertkun, M. Sawangphruk, N. Rubio and P. Sirisinudomkit, Microbubble synthesis of hybridised bacterial cellulose–gelatin separators for multifunctional supercapacitors, *Sustain. Energy Fuels*, 2025, **9**(7), 1745–1754, DOI: 10.1039/D4SE01684J.
7 J. Liu, H. Song, Z. Wang, J. Zhang, J. Zhang and X. Ba, Stretchable, self-healable, and reprocessable chemical cross-linked ionogels electrolytes based on gelatin for flexible supercapacitors, *J. Mater. Sci.*, 2020, **55**(9), 3991–4004, DOI: 10.1007/s10853-019-04271-4.
8 Y. Z. Zhang, Y. Wang, T. Cheng, L. Q. Yao, X. Li, W. Y. Lai, *et al.*, Printed supercapacitors: materials, printing and applications, *Chem. Soc. Rev.*, 2019, **48**(12), 3229–3264, DOI: 10.1039/C7CS00819H.
9 Z. Xia, T. Cai, X. Li, Q. Zhang, J. Shuai and S. Liu, Recent Progress of Printing Technologies for High-Efficient Organic Solar Cells, *Catalysts*, 2023, **13**(1), 156, DOI: 10.3390/catal13010156.
10 A. Teichler, J. Perelaer and U. S. Schubert, Inkjet printing of organic electronics – comparison of deposition techniques and state-of-the-art developments, *J Mater Chem C Mater*, 2013, **1**(10), 1910–1925, DOI: 10.1039/C2TC00255H.
11 X. Tang, K. Wu, X. Qi, H. jin Kwon, R. Wang, Z. Li, *et al.*, Screen Printing of Silver and Carbon Nanotube Composite Inks for Flexible and Reliable Organic Integrated Devices, *ACS Appl. Nano Mater.*, 2022, **5**(4), 4801–4811, DOI: 10.1021/acsanm.1c04317.
12 N. L. Vaklev, J. H. G. Steinke and A. J. Campbell, Gravure Printed Ultrathin Dielectric for Low Voltage Flexible Organic Field-Effect Transistors, *Adv. Mater. Interfaces*, 2019, **6**(11), 1900173, DOI: 10.1002/admi.201900173.
13 E. Pérez-Gutiérrez, J. Lozano, J. Gaspar-Tánori, J. L. Maldonado, B. Gómez, L. López, *et al.*, Organic solar cells all made by blade and slot–die coating techniques, *Sol. Energy*, 2017, **146**, 79–84, DOI: 10.1016/j.solener.2017.02.004.
14 G. Du, Z. Wang, T. Zhai, Y. Li, K. Chang, B. Yu, *et al.*, Flow-Enhanced Flexible Microcomb Printing of Organic Solar Cells, *ACS Appl. Mater. Interfaces*, 2022, **14**(11), 13572–13583, DOI: 10.1021/acsami.1c22724.
15 Y. Khan, A. Thielens, S. Muin, J. Ting, C. Baumbauer and A. C. Arias, A New Frontier of Printed Electronics: Flexible Hybrid Electronics, *Adv. Mater.*, 2020, **32**(15), 1905279, DOI: 10.1002/adma.201905279.
16 D. Batet, F. Vilaseca, E. Ramon, J. P. Esquivel and G. Gabriel, Experimental overview for green printed electronics: inks, substrates, and printing techniques, *Flexible Printed Electron.*, 2023, **8**(2), 024001, DOI: 10.1088/2058-8585/acd8cc.
17 X. Chen, R. Huang, Y. Han, W. Zha, J. Fang, J. Lin, *et al.*, Balancing the Molecular Aggregation and Vertical Phase Separation in the Polymer: Nonfullerene Blend Films Enables 13.09% Efficiency of Organic Solar Cells with Inkjet-Printed Active Layer, *Adv. Energy Mater.*, 2022, **12**(12), 2200044, DOI: 10.1002/aenm.202200044.
18 Y. Liu, C. Yang, T. Jiang, Y. Bao, L. Wang, D. Ji, *et al.*, A C6-DPA/PMMA binary blend ink for high-performance inkjet-printed organic field-effect transistors, *Mater Adv*, 2023, **4**(1), 302–306, DOI: 10.1039/D2MA00993E.
19 L. Zhan, S. Yin, Y. Li, S. Li, T. Chen, R. Sun, *et al.*, Multiphase Morphology with Enhanced Carrier Lifetime *via* Quaternary Strategy Enables High-Efficiency, Thick-Film, and Large-Area Organic Photovoltaics, *Adv. Mater.*, 2022, **34**(45), 2206269, DOI: 10.1002/adma.202206269.
20 F. Wu, Q. Zhu, J. Wang, W. Yang, S. Y. Jeong, L. Du, *et al.*, Conformationally locked polythiophene processed by room-temperature blade coating enables a breakthrough of the power factor, *J. Mater. Chem. A*, 2023, **11**(48), 26774–26783, DOI: 10.1039/D3TA04846B.
21 H. Zhao, H. B. Naveed, B. Lin, X. Zhou, J. Yuan, K. Zhou, *et al.*, Hot Hydrocarbon-Solvent Slot-Die Coating Enables High-Efficiency Organic Solar Cells with Temperature-Dependent Aggregation Behavior, *Adv. Mater.*, 2020, **32**(39), 2002302, DOI: 10.1002/adma.202002302.
22 C. Chae, Y. B. Kim, S. S. Lee, T. H. Kim, Y. Jo, H. S. Kim, *et al.*, All-3D-printed solid-state microsupercapacitors, *Energy Storage Mater*, 2021, **40**, 1–9, DOI: 10.1016/j.ensm.2021.04.038.
23 L. Sanchez-Duenas, E. Gomez, M. Larrañaga, M. Blanco, A. M. Goitandia, E. Aranzabe, *et al.*, A Review on Sustainable Inks for Printed Electronics: Materials for Conductive, Dielectric and Piezoelectric Sustainable Inks, *Materials*, 2023, **16**(11), 3940, DOI: 10.3390/ma16113940.
24 L. Y. Ma, N. Soin, S. N. Aidit, F. A. Md Rezali, M. Wan and S. F. Hatta, Recent advances in flexible solution-processed thin-film transistors for wearable electronics, *Mater. Sci. Semicond. Process.*, 2023, **165**, 107658, DOI: 10.1016/j.mssp.2023.107658.
25 D. Vak, K. Hwang, A. Faulks, Y. S. Jung, N. Clark, D. Y. Kim, *et al.*, 3D Printer Based Slot-Die Coater as a Lab-to-Fab Translation Tool for Solution-Processed Solar Cells, *Adv. Energy Mater.*, 2015, **5**(4), 1401539, DOI: 10.1002/aenm.201401539.
26 B. R. Hunde and A. D. Woldeyohannes, Modification of an extrusion-based 3D printing technology for thin-film printing for electronic device applications, *Int. J. Adv. Des. Manuf. Technol.*, 2024, **132**(11), 5537–5556, DOI: 10.1007/s00170-024-13588-7.
27 M. Idrees, S. Ahmed, Z. Mohammed, N. S. Korivi and V. Rangari, 3D printed supercapacitor using porous carbon derived from packaging waste, *Addit. Manuf.*, 2020, **36**, 101525, DOI: 10.1016/j.addma.2020.101525.
28 A. Khatkar, K. V. G, Y. Yadav, L. Khanam, R. Gupta and P. S. Singh. *Syringe Based Printer For Printing A Thin Film of*

Solution Processable Organic And/Or Inorganic Materials And A Method Thereof, India, 2023. p. 202111051417.

29 Y. Xiao, C. Zuo, J. X. Zhong, W. Q. Wu, L. Shen and L. Ding, Large-Area Blade-Coated Solar Cells: Advances and Perspectives, *Adv. Energy Mater.*, 2021, **11**(21), 2100378, DOI: **10.1002/aenm.202100378**.

30 Y. Li, H. Liu, J. Wu, H. Tang, H. Wang, Q. Yang, *et al.*, Additive and High-Temperature Processing Boost the Photovoltaic Performance of Nonfullerene Organic Solar Cells Fabricated with Blade Coating and Nonhalogenated Solvents, *ACS Appl. Mater. Interfaces*, 2021, **13**(8), 10239–10248, DOI: **10.1021/acsami.0c23035**.

31 G. Wang, M. A. Adil, J. Zhang and Z. Wei, Large-Area Organic Solar Cells: Material Requirements, Modular Designs, and Printing Methods, *Adv. Mater.*, 2019, **31**(45), 1805089, DOI: **10.1002/adma.201805089**.

32 R. Sun, Q. Wu, J. Guo, T. Wang, Y. Wu, B. Qiu, *et al.*, A Layer-by-Layer Architecture for Printable Organic Solar Cells Overcoming the Scaling Lag of Module Efficiency, *Joule*, 2020, **4**(2), 407–419, DOI: **10.1016/j.joule.2019.12.004**.

33 Q. Kang, L. Ye, B. Xu, C. An, S. J. Stuard, S. Zhang, *et al.*, A Printable Organic Cathode Interlayer Enables over 13% Efficiency for 1-cm2 Organic Solar Cells, *Joule*, 2019, **3**(1), 227–239, DOI: **10.1016/j.joule.2018.10.024**.

34 H. Zhao, L. Zhang, H. B. Naveed, B. Lin, B. Zhao, K. Zhou, *et al.*, Processing-Friendly Slot-Die-Cast Nonfullerene Organic Solar Cells with Optimized Morphology, *ACS Appl. Mater. Interfaces*, 2019, **11**(45), 42392–42402, DOI: **10.1021/acsami.9b12522**.

35 H. Fu, J. Peng, L. Xiang, Q. Zhang, X. Tan and Y. Lei, Enabling Scalable, Ultralow-Voltage Flexible Organic Field-Effect Transistors *via* Blade-Coated Cross-Linked Thick Polyvinyl Alcohol Gate Dielectric, *IEEE Trans. Electron Devices*, 2023, **70**(6), 3239–3244.

36 L. Zhang, B. Lin, B. Hu, X. Xu and W. Ma, Blade-Cast Nonfullerene Organic Solar Cells in Air with Excellent Morphology, Efficiency, and Stability, *Adv. Mater.*, 2018, **30**(22), 1800343, DOI: **10.1002/adma.201800343**.

37 B. Usmani and R. Ranjan, Inverted PTB7-Th:PC71BM organic solar cells with 11.8% PCE *via* incorporation of gold nanoparticles in ZnO electron transport layer, *Sol. Energy*, 2020, **214**, 220–230.

38 T. Anthopoulos, Significant Stability Enhancement in High-Efficiency Polymer:Fullerene Bulk Heterojunction Solar Cells by Blocking Ultraviolet Photons from Solar Light, *Advanced Science*, 2015, **3**(4), 1500269.

39 L. Khanam and S. P. Singh, Semitransparent organic solar cells based on low temperature processed PEIE as electron transport layer with enhanced charge transfer ability, *Phys. Scr.*, 2023, **98**(6), 065931, DOI: **10.1088/1402-4896/acd0de**.

40 A. S. Al-Ezzi and M. N. M. Ansari, Photovoltaic Solar Cells: A Review, *Appl. Syst. Innov.*, 2022, **5**(4), 67, DOI: **10.3390/asi5040067**.

41 L. Wu, H. Zang, Y. C. Hsiao, X. Zhang and B. Hu, Origin of the fill factor loss in bulk-heterojunction organic solar cells, *Appl. Phys. Lett.*, 2014, **104**(15), 153903, DOI: **10.1063/1.4871582**.

42 W. E. I. Sha, X. Li and W. C. H. Choy, Breaking the Space Charge Limit in Organic Solar Cells by a Novel Plasmonic-Electrical Concept, *Sci. Rep.*, 2014, **4**(1), 6236, DOI: **10.1038/srep06236**.

43 Y. Yadav and S. P. Singh, Effect of dielectric surface passivation on organic field-effect transistors: spectral analysis of the density of trap-states, *Semicond. Sci. Technol.*, 2022, **37**(1), 015015, DOI: **10.1088/1361-6641/ac3c97**.

44 M. R. Kiran, Y. Yadav and S. P. Singh, Threshold voltage tuning in gelatin biopolymer-gated high-performance organic field-effect transistors, *Synth. Met.*, 2023, **297**, 117398, DOI: **10.1016/j.synthmet.2023.117398**.

45 W. Y. Lee, J. Mei and Z. Bao. OFETs: Basic concepts and material designs. In: *The WSPC Reference on Organic Electronics: Organic Semiconductors*, pp. 19–83, **https://www.worldscientific.com/doi/abs/10.1142/9789813148611_0002**.

46 J. Chang, Z. Lin, C. Zhang and Y. Hao. Organic Field-Effect Transistor: Device Physics, Materials, and Process, in *Different Types of Field-Effect Transistors*, ed. Pejovic M. M. and Pejovic M. M., Rijeka: IntechOpen, 2017, Ch. 7, DOI: **10.5772/intechopen.68215**.

47 S. M. Sze, Y. Li and K. K. Ng, *Physics of Semiconductor Devices*, John wiley & sons, 2021.

48 E. P. Vandamme, P. Jansen and L. Deferm, Modeling the subthreshold swing in MOSFET's, *IEEE Electron Device Lett.*, 1997, **18**(8), 369–371.

49 M. McDowell, I. G. Hill, J. E. McDermott, S. L. Bernasek and J. Schwartz, Improved organic thin-film transistor performance using novel self-assembled monolayers, *Appl. Phys. Lett.*, 2006, **88**(7), 073505, DOI: **10.1063/1.2173711**.

50 Y. Hu, P. Wei, X. Wang, L. Bu and G. Lu, Giant Transconductance of Organic Field-Effect Transistors in Compensation Electric Fields, *Phys. Rev. Appl.*, 2018,10, **5**, 54024, DOI: **10.1103/PhysRevApplied.10.054024**.

51 S. D. Wang, Y. Yan and K. Tsukagoshi, Transition-Voltage Method for Estimating Contact Resistance in Organic Thin-Film Transistors, *IEEE Electron Device Lett.*, 2010, **31**(5), 509–511.

52 W. S. C. Roelofs, W. Li, R. A. J. Janssen, D. M. de Leeuw and M. Kemerink, Contactless charge carrier mobility measurement in organic field-effect transistors, *Org. Electron.*, 2014, **15**(11), 2855–2861, DOI: **10.1016/j.orgel.2014.08.027**.

53 Q. Wang, S. Jiang, Y. Shi and Y. Li, Effect of access resistance on the experimentally measured temperature–carrier mobility dependence in highly-crystalline DNTT-based transistors, *Mater Adv*, 2020, **1**(6), 1799–1804, DOI: **10.1039/D0MA00530D**.

54 Y. Zhou, K. Zhang, Z. Chen and H. Zhang, Molecular Design Concept for Enhancement Charge Carrier Mobility in OFETs: A Review, *Materials*, 2023, **16**(20), 89–6645, DOI: **10.3390/ma16206645**.

55 S. Yang, S. Park, J. Bintinger, Y. Bonnassieux, J. Anthony and I. Kymissis, Employing Pneumatic Nozzle Printing for Controlling the Crystal Growth of Small Molecule Organic

Semiconductor for Field-Effect Transistors, *Adv. Electron. Mater.*, 2018, **4**(6), 1700534, DOI: **10.1002/aelm.201700534**.

56 N. Korivi, R. Mahbub, Z. Ahmadi, S. Azadehranjbar, J. E. Shield, Y. Ni, *et al.*, 3D printed elastomer ternary composites, *Electron. Lett.*, 2023, **59**(8), e12749, DOI: **10.1049/ell2.12749**.

57 S. Sahoo, A. Yadav and V. Rangari, Surface tailored spent coffee ground derived carbon reinforced waste HDPE composites for 3D printing application, *Compos., Part C: Open Access*, 2025, **16**, 100570, DOI: **10.1016/j.jcomc.2025.100570**.

58 Y. Jo, J. H. Hwang, S. S. Lee, S. Y. Lee, Y. S. Kim, D. G. Kim, *et al.*, Printable Self-Activated Liquid Metal Stretchable Conductors from Polyvinylpyrrolidone-Functionalized Eutectic Gallium Indium Composites, *ACS Appl. Mater. Interfaces*, 2022, **14**(8), 10747–10757, DOI: **10.1021/acsami.1c20185**.

59 Y. Jo, J. Y. Kim, S. Jung, B. Y. Ahn, J. A. Lewis, Y. Choi, *et al.*, 3D polymer objects with electronic components interconnected *via* conformally printed electrodes, *Nanoscale*, 2017, **9**(39), 14798–14803, DOI: **10.1039/C7NR04111J**.